

Quantum control of qubits and atomic motion using ultrafast laser pulses

J. Mizrahi · B. Neyenhuis · K. G. Johnson ·
W. C. Campbell · C. Senko · D. Hayes ·
C. Monroe

Received: 1 July 2013 / Accepted: 25 October 2013
© Springer-Verlag Berlin Heidelberg 2013

Abstract Pulsed lasers offer significant advantages over continuous wave (CW) lasers in the coherent control of qubits. Here we review the theoretical and experimental aspects of controlling the internal and external states of individual trapped atoms with pulse trains. Two distinct regimes of laser intensity are identified. When the pulses are sufficiently weak that the Rabi frequency Ω is much smaller than the trap frequency ω_{trap} , sideband transitions can be addressed and atom-atom entanglement can be accomplished in much the same way as with CW lasers. By contrast, if the pulses are very strong $\Omega \gg \omega_{\text{trap}}$, impulsive spin-dependent kicks can be combined to create entangling gates which are much faster than a trap period. These fast entangling gates should work outside of the Lamb-Dicke regime and be insensitive to thermal atomic motion.

1 Introduction

Over the past decade, frequency combs from mode-locked lasers have become an essential tool in the field of optical frequency metrology [1–4]. This is due to the broad spectrum of lines spaced by the pulse repetition rate present in a frequency comb. This allows it to serve as a precise connection between distant frequencies. In the context of

metrology, this feature is used as a ruler in which the spacings between comb lines serve as tick marks. In the context of coherent control, this feature can be used to directly bridge large frequency gaps between energy levels in a controllable way. This technique has been used effectively to control diverse quantum systems, including multilevel atoms [5], molecules [6], semiconductor spin states [7, 8], and ions [9–11]. Mode-locked lasers therefore have a bright future as a tool for qubit manipulation in a number of different quantum computer architectures.

Trapped atomic ions are a very promising medium for quantum information, due to their extremely long coherence times, well-established means for coherent control and manipulation, and potential for scalability [12, 13]. High-fidelity entanglement of ions is now routinely achieved [14–17], as well as implementations of schemes for analog quantum simulation [18–20] and digital quantum algorithms [21–23]. However, obstacles remain before a trapped ion quantum computer can outperform a classical computer. Technical limitations to gate fidelity include laser-induced decoherence [24, 25] and ion heating [26]. Existing gates are also typically limited in the number of ions which can be manipulated in a single chain. This is because these gates rely on addressing normal modes of motion of the ion chain [27, 28]. As the number of ions grows, the density of normal modes in frequency space grows as well, making it increasingly difficult to avoid undesired couplings. This increased mode density slows down the gate, increasing sensitivity to low-frequency noise.

High-power mode-locked lasers offer one potential solution to some of these issues (there are a number of other approaches, see [29–32]). The goal of this paper is to discuss recent work on the interaction between trapped ions and mode-locked laser pulses.

J. Mizrahi (✉) · B. Neyenhuis · K. G. Johnson · C. Senko ·
D. Hayes · C. Monroe
Department of Physics and National Institute of Standards
and Technology, Joint Quantum Institute, University
of Maryland, College Park, College Park, MD 20742, USA
e-mail: mizrahi.jonathan@gmail.com

W. C. Campbell
Department of Physics and Astronomy, University of California,
Los Angeles, Los Angeles, CA 90095, USA

From a technical standpoint, the large bandwidth inherent in a comb eliminates some of the complexity and expense of driving Raman transitions. For hyperfine qubits in ions, the frequency splitting is typically several GHz. Bridging this gap with CW beams requires either two separate phase-locked lasers or a high-frequency EOM (which is typically inefficient). By contrast, a single mode-locked laser can directly drive the transition without any high-frequency shifts. Moreover, it is not necessary to stabilize either the carrier-envelope phase or the repetition rate of the mode-locked laser, as will be discussed later. This enables the use of commercially available, industrial lasers.

As a second advantage, the large instantaneous intensity present in a single pulse enables efficient harmonic generation. For this reason, high-power UV lasers are readily obtainable at frequencies appropriate for trapped ion control. High power enables operating with a large detuning, which suppresses laser-induced decoherence. High power also enables motion control in a time significantly faster than the trap period, which is a new regime in trapped ion control. It should allow the implementation of theoretical proposals for ultrafast gates which are independent of ion temperature, as discussed in Sect. 4.

This paper is divided into three parts. Section 2 describes spin control of an ion with a pulse train, without motional coupling. Section 3 introduces spin–motion coupling. Section 4 explains how to realize an ultrafast two ion gate using fast pulses.

1.1 Experimental system

We take the atomic qubit as composed of stable ground-state electronic levels separated by RF or microwave frequencies. The schemes reported here can be extended to the case of qubit levels separated by optical intervals, but for concreteness we will concentrate on qubits stored in hyperfine or Zeeman levels in the ground state of an alkali-like atom.

In order to effectively use laser pulses for qubit control, we require three frequency scales to be well separated. Let τ denote the pulse duration. The pulse bandwidth $1/\tau$ should be much larger than the qubit splitting ω_q so that the two qubit levels are coupled by the optical field, yet it should be much smaller than the detuning Δ from the excited state so that it is negligibly populated during the interaction. Note also that the detuning Δ should not be much larger than the fine structure splitting in an alkali-like atom; otherwise, the Raman coupling is suppressed [16]. For many atomic systems, the condition $\omega_q \ll 1/\tau \ll \Delta$ is satisfied for a range of laser pulse durations $0.5 \text{ ps} \lesssim \tau \lesssim 25 \text{ ps}$.

Here we consider the interaction between ultrafast laser pulses and qubits represented by laser-cooled $^{171}\text{Yb}^+$ ions confined in an RF Paul trap, although many of the results

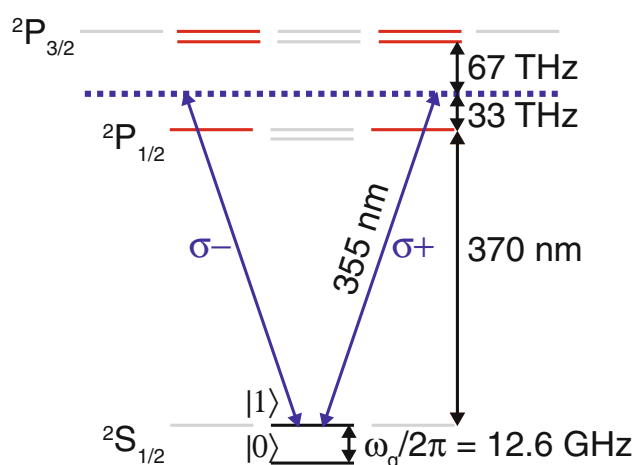


Fig. 1 Relevant energy levels of $^{171}\text{Yb}^+$. The qubit is identified with the two $m_F = 0$ states in the ground-state manifold. Continuous wave 369 nm light is used for cooling, detection, and optical pumping. Laser pulses at 355 nm are used for qubit manipulation, driving stimulated Raman transitions between the qubit levels from σ_{\pm} polarized light

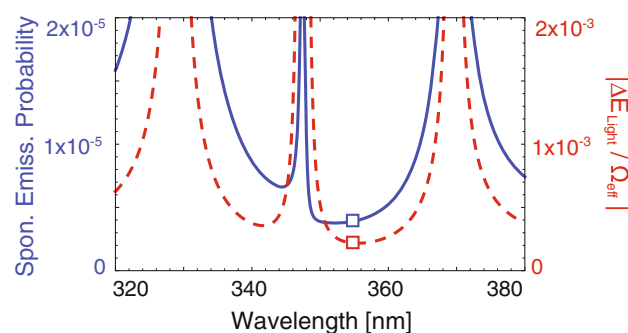


Fig. 2 Theoretical curves showing sources of laser-induced decoherence as a function of wavelength. Solid blue line is spontaneous emission probability during a π pulse as a function of laser wavelength. Dashed red line is differential AC Stark shift divided by Rabi frequency as a function of laser wavelength. White squares are at 355 nm, where both curves are near a minimum

discussed herein are applicable in a range of contexts involving ultrafast pulses on the internal and external degrees of freedom of optically coupled qubits. The qubit levels are defined by the $m_F = 0$ states of the $^2S_{1/2}$ hyperfine manifold of $^{171}\text{Yb}^+$: $|F = 0, m_F = 0\rangle \equiv |0\rangle, |F = 1, m_F = 0\rangle \equiv |1\rangle$. The qubit frequency splitting is $\omega_q/2\pi = 12.6 \text{ GHz}$. Doppler cooling of atomic motion, and initialization/detection of the qubit are all accomplished using continuous wave (CW) beams near 369 nm [33].

We consider optical pulses generated from a mode-locked, tripled, Nd:YVO₄ laser at 355 nm to drive stimulated Raman transitions between the qubit states $|0\rangle$ and $|1\rangle$, that may also be accompanied by optical dipole forces. Typical laser repetition rates are in the range $\omega_{\text{rep}}/$

$2\pi = 80\text{--}120$ MHz, with a pulse duration $\tau \sim 10$ ps (~ 100 GHz bandwidth) and maximum average power \bar{P} of several Watts (pulse energies of up to 100 nJ). This light is detuned by $\Delta_{1/2} \approx +33$ THz from the excited ${}^2P_{1/2}$ level, and $\Delta_{3/2} \approx -67$ THz from the ${}^2P_{3/2}$ level, as shown in Fig. 1. This wavelength and pulse duration are nearly optimal for controlling the ${}^{171}\text{Yb}^+$ system, exhibiting minimal spontaneous emission and differential AC Stark shifts [10], as shown in Fig. 2.

2 Spin control with pulses

2.1 Strong pulses

Consider the interaction of a train of pulses with an atom, as shown in Fig. 3. After performing a rotating wave approximation at the optical frequency and adiabatically eliminating the excited P states, the effective Hamiltonian for the interaction becomes [10]:

$$H = -\frac{\omega_q}{2}\hat{\sigma}_z - \frac{\Omega(t)}{2}\hat{\sigma}_x \tag{1}$$

where ω_q is the qubit splitting, $\hat{\sigma}_{z,x}$ are Pauli spin operators, and $\Omega(t) = g(t)^2/2\Delta$ is the two-photon Rabi frequency for pure σ^+ or σ^- polarized light. Here, the single-photon $S - P$ resonant coupling strength $g(t) = \gamma\sqrt{I(t)/2I_{\text{sat}}}$ with effective detuning given by $1/\Delta = 1/\Delta_{1/2} - 1/\Delta_{3/2}$, accounting for both excited states. $I(t)$ is time-dependent intensity of the pulse. In the ${}^{171}\text{Yb}^+$ system, $I_{\text{sat}} = 0.15$ W/cm² is the saturation intensity for the ${}^2S_{1/2} - {}^2P_{1/2}$ transition and the ${}^2P_{1/2}$ state linewidth is $\gamma/2\pi = 19.6$ MHz.

We note that the above Hamiltonian can be generalized to include the effect of ultrafast pulses connecting the qubit levels to a third (transiently populated) level on resonance, or in the case of qubits with an optical splitting, directly on resonance with the qubit levels [34]. In addition, by choosing appropriate qubit levels and laser pulse polarization, a generalization of the above interaction can produce a differential Stark shift instead of a transition between the levels, in which case the $\hat{\sigma}_x$ coupling term above is replaced by $\hat{\sigma}_z$ [34]. In this case, the actual implementation of entangling gates between multiple qubits through collective motion is not exactly as described below, although there are many similarities. It should also be noted that qubit states

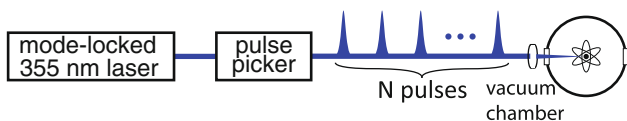


Fig. 3 A fast pulse picker selects a train of N circularly polarized pulses, each with area θ . These pulses drive stimulated Raman transitions in a trapped ion

that have sizable differential AC Stark shift are also first-order sensitive to external magnetic fields [16] and hence perform as relatively poor qubit memories.

For a single pulse ($N = 1$) with either σ_{\pm} polarization, the time dependence of the Rabi frequency originates from the intensity profile of the laser $I(t)$, which for a mode-locked laser pulse can be accurately modelled by a squared hyperbolic secant envelope [35]. Intensity envelope functions of externally generated optical harmonics of the fundamental laser field should be higher powers of the sech function. However, their shape remains quite similar to that of the sech function. We therefore approximate the pulse intensity as $I(t) = I_0 \text{sech}(\frac{\pi t}{\tau})$ with peak laser intensity I_0 and pulse duration τ , having FWHM in time of 0.838τ . This approximation allows a simple analytic solution to the evolution of the above Hamiltonian, and numerical simulation indicates that this is at most a 1–2 % correction to everything presented here.

The qubit Rabi frequency can therefore be written as:

$$\Omega(t) = \frac{\theta}{\tau} \text{sech}\left(\frac{\pi t}{\tau}\right), \tag{2}$$

where $\theta = \int \Omega(t)dt$ is the pulse area. For the Raman transition considered here in the ${}^{171}\text{Yb}^+$ system using light tuned to 355 nm, we have [9]:

$$\theta = \frac{I_0\tau\gamma^2}{2I_{\text{sat}}\Delta} \tag{3}$$

Alternatively, θ can be expressed in terms of the average intensity of the laser \bar{I} and the repetition frequency ω_{rep} using the relation $I_0\tau = 2\pi\bar{I}/\omega_{\text{rep}}$. We find that to drive a Raman π -pulse with a single laser pulse focussed to a Gaussian waist w ($1/e$ field radius), the required pulse energy is $\mathcal{E}_{\pi} = \pi I_0 w^2 \tau / 2 = \pi^2 I_{\text{sat}} w^2 \Delta / \gamma^2$. For the ${}^{171}\text{Yb}^+$ system using a 355-nm beam focused to a waist of $w = 10$ μm , we find $\mathcal{E}_{\pi} \sim 12$ nJ.

The Hamiltonian of Eqs. 1 and 2 for the hyperbolic secant Rabi frequency envelope in time was solved exactly by Rosen and Zener [36]. For the purposes of this analysis, we are not interested in the dynamics during the pulse, but only the resultant state after the pulse. The evolution operator for a pulse followed by free evolution for a time T is given by [37, 38]:

$$U = \begin{pmatrix} A & iB^* \\ iB & A^* \end{pmatrix} \tag{4}$$

where A and B are given by:

$$A = \frac{\Gamma^2(\xi)e^{i\omega_q T/2}}{\Gamma(\xi - \frac{\theta}{2\pi})\Gamma(\xi + \frac{\theta}{2\pi})} \tag{5}$$

$$B = -\sin\left(\frac{\theta}{2}\right) \text{sech}\left(\frac{\omega_q \tau}{2}\right) e^{-i\omega_q T/2} \tag{6}$$

$$\xi = \frac{1}{2} + i \frac{\omega_q \tau}{2\pi} \tag{7}$$

where $\Gamma(\xi)$ is the gamma function. For a fixed value of θ , this evolution operator can be written as a pure rotation operator:

$$\tilde{U} = e^{i\varphi \hat{n} \cdot \vec{\sigma}/2} \tag{8}$$

where the rotation axis \hat{n} and rotation angle φ are given by:

$$\cos\left(\frac{\varphi}{2}\right) = \text{Re}(A) \tag{9}$$

$$n_z \sin\left(\frac{\varphi}{2}\right) = \text{Im}(A) \tag{10}$$

$$(n_x + in_y) \sin\left(\frac{\varphi}{2}\right) = B \tag{11}$$

The equivalent pure Bloch sphere rotation is shown in Fig. 4b. Equation 8 allows the evolution operator to quickly be extended to N pulses equally spaced by a time T :

$$U_N = e^{iN\varphi \hat{n} \cdot \vec{\sigma}/2} \tag{12}$$

If the ion is initialized to the state $|0\rangle$, then the transition probability after N pulses is given by:

$$P_{0 \rightarrow 1} = \left| i \sin\left(\frac{N\varphi}{2}\right) (n_x + in_y) \right|^2 = \left(\frac{|B|^2}{\sin^2\left(\frac{\varphi}{2}\right)} \right) \sin^2\left(\frac{N\varphi}{2}\right) \tag{13}$$

To understand the behavior described by the above equations, first consider the limit of an infinitesimally short pulse: $\tau = 0$. In that case, Eqs. 5 and 6 become:

$$A = \cos\left(\frac{\theta}{2}\right) e^{i\omega_q T/2} \tag{14}$$

$$B = -\sin\left(\frac{\theta}{2}\right) e^{i\omega_q T/2} \tag{15}$$

If the time between pulses satisfies the condition:

$$\omega_q T = 2\pi n, n \in \mathbb{Z} \tag{16}$$

then Eqs. 9, 10, and 11 show that $\varphi = \theta$, $n_z = n_y = 0$, and $n_x = 1$. In this case, the action of each pulse is rotation about the x -axis, by an angle equal to the pulse area. Equation 13 then becomes:

$$P_{0 \rightarrow 1} = \sin^2\left(\frac{N\theta}{2}\right) \tag{17}$$

This equation shows that the behavior is discretized Rabi flopping.

Now consider nonzero pulse duration. Equation 13 shows that for $N = 1$, the transition probability reduces to:

$$P_{0 \rightarrow 1} = |B|^2 = \sin^2(\theta/2) \text{sech}^2(\omega_q \tau/2) \tag{18}$$

Therefore, for a single pulse, the maximum population transferred is $\text{sech}^2(\omega_q \tau/2)$. This quantity is always less than one, meaning a single pulse cannot fully flip the spin of the qubit. However, for two pulses, Eq. 13 can be made equal to 1, for particular values of the delay time T . If $T \ll 1/\omega_q$, then the correct delay condition will be a small correction to Eq. 16.

This can be understood by examining the qubit evolution on the Bloch sphere. The Bloch sphere path for the Rosen-Zener solution is shown as a function of θ in Fig. 4a. Note that the path is twisted—for small values of θ , the rotation axis is nearly purely about the x -axis. As θ increases, the amount of z -rotation also increases. If θ is fixed, the final state can be connected to the initial state by a pure rotation, which is shown in Fig. 4b. For nonzero pulse duration, the rotation axis is never purely in the x - y plane, meaning the north pole of the Bloch sphere is never reached. However, two pulses can fully flip the spin, so long as one pulse can reach the equator, as shown in Fig. 4e. For $^{171}\text{Yb}^+$, the condition for two pulses to be able to fully transfer population is $\tau < 22$ ps.

These results show that two fast pulses can be used to rotate the state of a qubit extremely rapidly, in less than one qubit period. Moreover, these same pulses can be used to rotate the phase of a qubit (i.e., z -rotations on the Bloch sphere). To see this, again consider a pair of pulses as above. However, instead of choosing a delay such that Eq. 13 equals 1, a delay is chosen such that it equals 0; i.e., $\varphi = \pi$. In that case, the evolution operator causes a phase shift of the qubit, controllable via the power of the pulses.

Figure 4d shows experimental results for a single pulse. The datasets shown correspond to two different lasers with different pulse durations. The circles shows a maximum brightness of 72 %, corresponding to a pulse duration of $\tau = 14.8$ ps in Eq. 18. The squares shows a maximum of 91 %, corresponding to $\tau = 7.6$ ps. These numbers are consistent with independent measurements of the pulse duration.

Figure 4f shows the results of scanning the delay between two pulses. The two pulses were created by splitting a single pulse from the laser and directing the two halves of the pulse onto the ion from opposite directions, as described in [10]. (Note that while the pulses are directed onto the ion from opposite directions, there is no coupling to the ion’s motion—the pulses are not overlapped in time. There is therefore no possibility of momentum transfer.) The maximum occurs at a delay of 72 ps, approximately one qubit period. It is slightly less than one qubit period due to the off-axis rotation caused by the nonzero pulse duration, as shown on the Bloch sphere in Fig. 4e. The maximum is less than one due to detection errors.

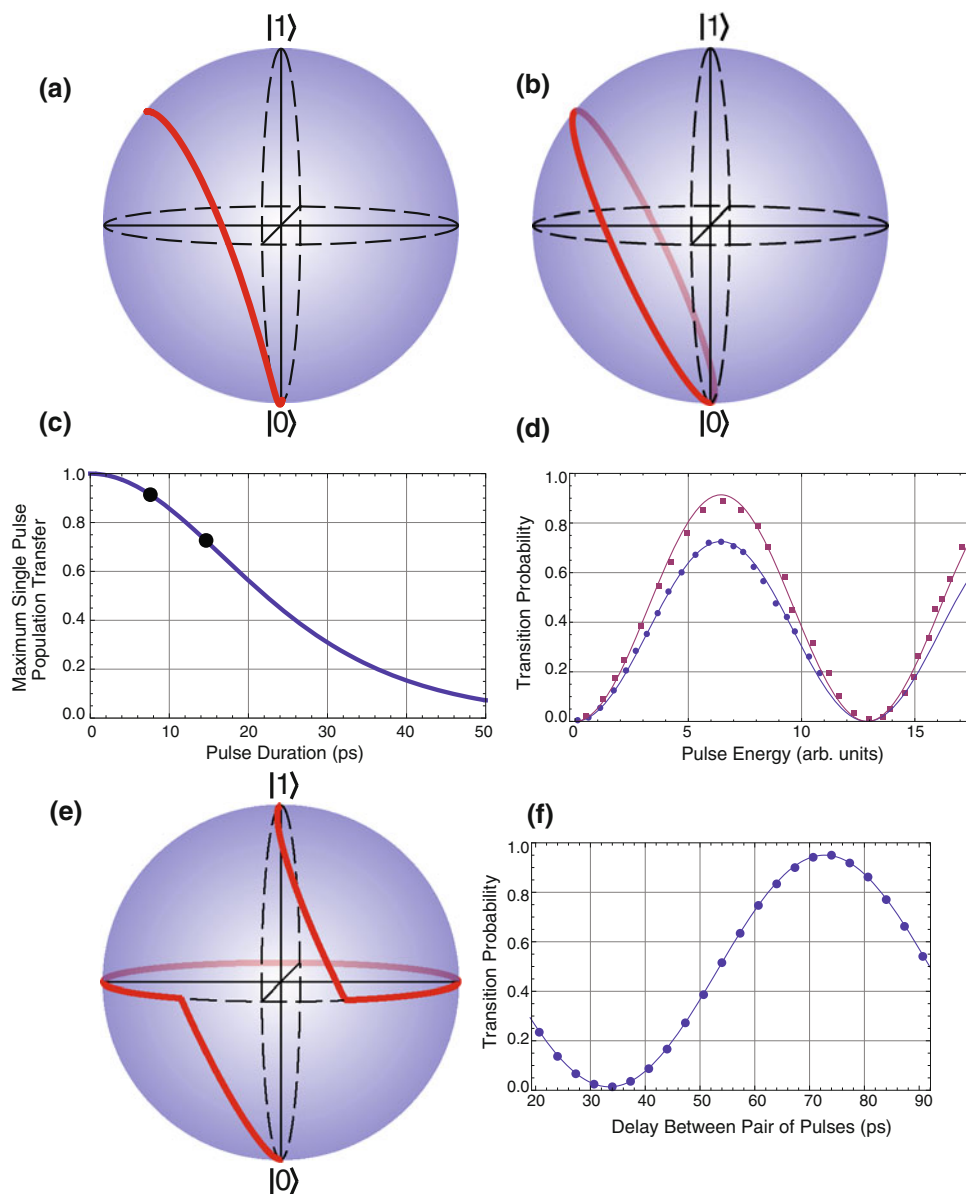


Fig. 4 **a** Bloch sphere position as a function of pulse energy, following the Rosen–Zener solution in Eqs. 5–7. **b** The final position reached by the twisted path in **a** can be represented by a single effective rotation axis and angle, as in Eq. 8. The angle of rotation is given by φ ; the axis is determined by θ and τ . **c** Theoretical maximum population transfer in $^{171}\text{Yb}^+$ for a single pulse as a function of pulse duration, based on Eq. 18. The *black dots* indicate the points corresponding to the data in **(d)**. **d** Experimental data showing the behavior described theoretically in **(a–c)**. Ion state is measured as a function of incident pulse energy. The transfer probability reaches a maximum given by Eq. 18. The two different datasets correspond to

two different lasers with different pulse durations. The fit to the data show that those pulse durations are 14.7 ps (*circles*) and 7.6 ps (*squares*). These points are indicated on the plot in **(c)**. **e** Two identical pulses separated by an appropriate delay can fully transfer the population. Each pulse has sufficient energy to rotate the state to the equator of the Bloch sphere. The appropriate delay is approximately the qubit cycle time $2\pi/\omega_q$. It is slightly smaller due to the off-axis rotation caused by the Rosen–Zener dynamics. **f** Data showing the effect in **(e)**. As the delay between the pulses is scanned, the transition probability goes from 0 to 1. The maximum is less than one due to detection errors

To demonstrate pure phase rotation, the delay between the pulses was set such that there was no net population transfer (34 ps delay in Fig. 4f). This pulse pair was then put between two $\pi/2$ Ramsey zones, and the frequency of those Ramsey zones scanned for different laser intensities. The phase shift caused by the laser pulses manifests as a

shift in the Ramsey fringes. The angle of z -rotation can then be calculated based on the shift. The amount of phase rotation is set by controlling the intensity of the two pulses. The results are shown in Fig. 5. The fit curve in **(c)** is derived from the Rosen–Zener solution, Eqs. 5–7. The only free parameter is the overall scaling, i.e., the

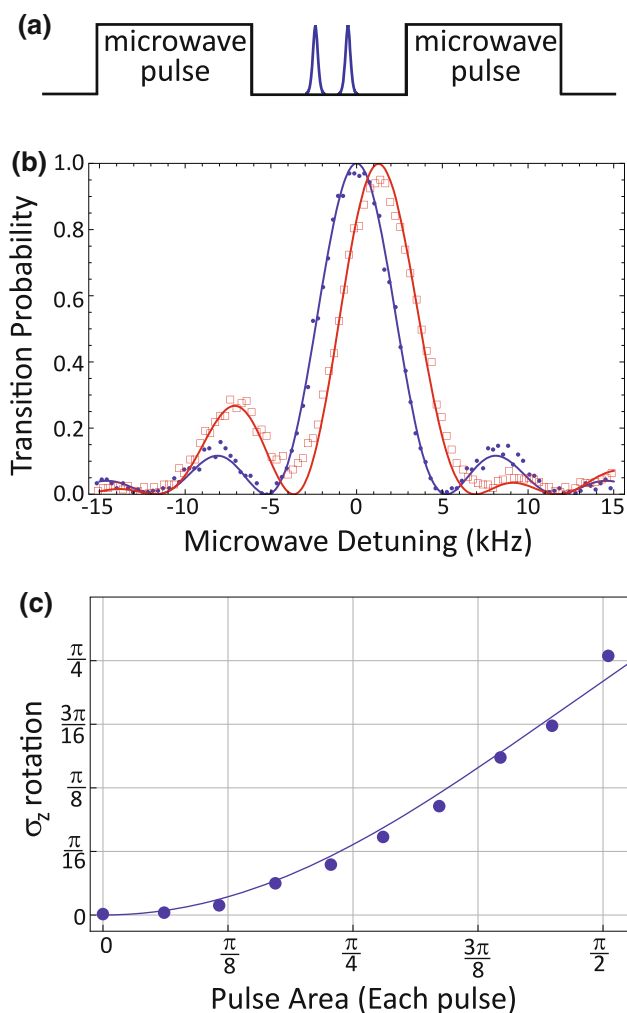


Fig. 5 Data showing fast phase rotation caused by pair of pulses. **a** Ramsey sequence: the frequency of two microwave $\pi/2$ pulses is scanned. In between the microwaves, two fast laser pulses with delay set to cancel x -rotation are inserted. Fringe shift is then measured as a function of pulse area. **b** Data showing fringe shift. *Circles* No laser pulses, *Squares* Laser pulses of pulse area equal to 1.25, showing phase rotation angle of 0.49. **c** Measured z -rotation angle as a function of pulse area

correspondence between the measured pulse amplitude and the pulse area θ on the x -axis of the plot.

These results show that by controlling the intensity and delay between two fast pulses, any arbitrary Bloch sphere rotation can be achieved in tens of picoseconds.

2.2 Weak pulses

In the above section, the pulse area was large, such that a single pulse had a significant effect on the qubit state. If instead the area per pulse is small ($\theta \ll 1$), then many pulses are required to coherently drive the qubit substantially. In this case, the analysis is better understood in the frequency

domain. The Fourier transform of a train of equally spaced pulses with a fixed phase relationship is a frequency comb, with teeth spaced by the repetition frequency ω_{rep} . The width of an individual tooth in an N pulse train scales like ω_{rep}/N . If the width of a tooth is small compared to the tooth spacing ($N \gg 1$), then the comb can be thought of as an ensemble of CW lasers. All that remains is to ensure that the frequency comb spectrum includes optical beat notes that are resonant with the qubit splitting ω_q .

Note that since the qubit transitions are driven by a frequency difference between comb lines rather than by an absolute optical frequency, the carrier-envelope phase (CEP) is therefore irrelevant and does not need to be stabilized. However, in order to coherently drive the qubit, it is important that the beat note at the qubit splitting be stable. In general, well-designed mode-locked lasers enjoy excellent passive stability of their repetition rate (comb tooth spacing) over the time scale of a coherent qubit operation (microseconds), so that individual operations are coherent. Over longer times, however, drifts in the repetition rate will spoil attempts to signal average or concatenate operations. The fractional drift of the repetition rate, similar to the fractional linewidth and drift of a free-running CW laser, is typically in the range of $\sim 10^{-7}$ over minutes. This drift can be eliminated by actively stabilizing the laser repetition rate, using a piezo-mounted end mirror [9].

2.2.1 Single comb

A single comb of equally spaced components can drive stimulated Raman transitions if the qubit splitting is an integer multiple of the comb teeth spacing, as shown in Fig. 6a:

$$\omega_q = n\omega_{\text{rep}}, n \in \mathbb{Z} \tag{19}$$

This condition is equivalent to Eq. 16. The Rabi frequency can be computed by summing the effect of all pairs of comb teeth separated by ω_q [9]. For two CW phase-locked beams with single-photon Rabi frequencies g_1 and g_2 (assumed to be real), the Raman Rabi frequency between qubit states is $\Omega = g_1 g_2 / 2\Delta$. For an optical frequency comb resulting from hyperbolic secant pulses, the k th comb tooth at frequency $k\omega_{\text{rep}}$ from the optical carrier has single-photon Rabi frequency

$$g_k = g_0 \sqrt{\frac{\omega_{\text{rep}}\tau}{2}} \text{sech}(k\omega_{\text{rep}}\tau), \tag{20}$$

where $g_0^2 = \sum_{k=-\infty}^{+\infty} g_k^2 = (\bar{I}/2I_{\text{sat}})\gamma^2$. The net two-photon Rabi frequency from the frequency comb is therefore

$$\Omega = \sum_{k=-\infty}^{+\infty} \frac{g_k g_{k+n}}{2\Delta} \tag{21}$$

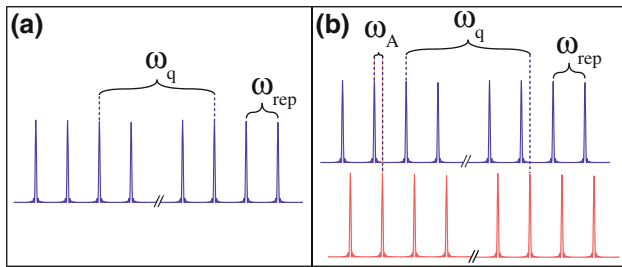


Fig. 6 **a** One frequency comb can drive Raman transitions if pairs of comb lines are separated by the qubit frequency, leading to the condition in Eq. 19. **b** Two frequency combs can drive Raman transitions together if a frequency offset ω_A between the combs causes lines from the separate beams to be spaced by the qubit frequency, leading to the condition in Eq. 29

$$\approx \Omega_0 \operatorname{sech}\left(\frac{\omega_q \tau}{2}\right), \quad (22)$$

where n is the number of comb teeth spanning the qubit splitting (Eq. 19), $\Omega_0 = g_0^2/2\Delta$ and we assume the beat notes at ω_q all add in phase since the pulse has negligible frequency chirp. The remaining hyperbolic secant factor is nearly unity when the individual pulse bandwidth $1/\tau$ is much greater than the qubit frequency splitting ω_q .

This expression can be connected to the time domain analysis above in a straightforward manner. In Eq. 13, the number of pulses N can be replaced by time t using the relation $N = 2\pi\omega_{\text{rep}} t$. This shows that the Rabi frequency is related to the rotation angle φ by:

$$\Omega = 2\pi\omega_{\text{rep}}\varphi \quad (23)$$

Equation 13 also shows that full contrast requires $\sin^2(\varphi/2) = B^2$, which is equivalent to the condition that the comb is driving the transition on resonance. This relation becomes:

$$\sin^2\left(\frac{\varphi}{2}\right) = \sin^2\left(\frac{\theta}{2}\right) \operatorname{sech}^2\left(\frac{\omega_q \tau}{2}\right) \quad (24)$$

$$\Rightarrow \varphi \approx \theta \operatorname{sech}\left(\frac{\omega_q \tau}{2}\right) \quad (25)$$

$$\Rightarrow \Omega = \Omega_0 \operatorname{sech}\left(\frac{\omega_q \tau}{2}\right) \quad (26)$$

The second line follows from the small angle approximation, and the third line is the second multiplied by $2\pi\omega_{\text{rep}}$. This shows that the constant $\Omega_0 = 2\pi\omega_{\text{rep}}\theta$. From this, it is clear that the approximation made in treating the pulse train as an ensemble of CW lasers is equivalent to the assumption that the effect of an individual pulse is small.

In addition to the resonant beat note at the qubit frequency, there will also be many beat notes at integer multiples of ω_{rep} away from the qubit frequency from the multitude of comb teeth splittings. These other beat notes will lead to a shift in the qubit resonance and can be

thought of as a higher-order four-photon AC Stark shift. From Eq. 22, the strength of the beat note at $j\omega_{\text{rep}}$ is characterized by its resonant Rabi frequency $\Omega_j \approx \Omega_0 \operatorname{sech}(j\omega_{\text{rep}}\tau/2)$. The net four-photon Stark shift is then a sum over all non-resonant beat notes,

$$\delta_4 = - \sum_{\substack{j=-\infty \\ j \neq n}}^{\infty} \frac{\Omega_j^2}{2(j\omega_{\text{rep}} - \omega_q)} \quad (27)$$

$$= - \frac{\Omega_0^2}{2\omega_{\text{rep}}} \sum_{\substack{j=-\infty \\ j \neq 0}}^{\infty} \frac{\operatorname{sech}^2[(j+n)\omega_{\text{rep}}\tau/2]}{j} \\ \approx \left(\frac{7\zeta(3)}{\pi^2}\right) \frac{\Omega_0^2 \omega_q \tau}{\omega_{\text{rep}}} \quad (28)$$

where ζ is the Riemann zeta function. The last expression is valid in the case where $\omega_{\text{rep}}\tau \ll 1$ and to lowest order in $\omega_q\tau/2$. For laser pulses of $\tau = 10$ ps duration with a repetition rate $\omega_{\text{rep}}/2\pi = 80$ MHz and net Rabi frequency $\Omega/2\pi = 1$ MHz, for the $^{171}\text{Yb}^+$ qubit we find a resultant 4-photon Stark shift of $\delta_4/2\pi \approx +8.5$ kHz. It should be noted that Eq. 28 could also be derived from the time domain Rosen-Zener solution discussed in Sect. 2.1 [39].

2.2.2 Two combs

Equation 19 requires a laser with a repetition rate that is commensurate with the qubit splitting. However, this may be difficult to achieve in practice, and in any case it is undesirable for non-copropagating laser pulses—such a laser cannot generate the spin-dependent forces discussed in Sect. 3. Moreover, the repetition rate on many mode-locked lasers cannot be easily controlled to stabilize drifts. It is therefore convenient to generate two combs, with one frequency shifted relative to the other, typically via an AOM as shown in Fig. 6b. In this way, Raman transitions are controlled through this frequency offset and this configuration allows atomic forces to be exerted in a given direction when tuned near motional sideband transitions (see Sect. 3). Finally, drifts in the repetition rate can be measured and fed forward onto a downstream modulator, in case the repetition rate of a laser is not accessible. This feed-forward effectively eliminates drift in the relevant comb beat note to drive qubit transitions by 29, as the “breathing” of the comb teeth is compensated by the offset comb [40].

Including an offset frequency ω_A between the two combs, the condition for driving transitions now becomes:

$$\omega_q = n\omega_{\text{rep}} \pm \omega_A, n \in \mathbb{Z} \quad (29)$$

In order to allow for the possibility of spin-dependent forces in a counterpropagating geometry, we exclude the offset frequency values $\omega_A = k\omega_{\text{rep}}$ or $(k+1/2)\omega_{\text{rep}}$,

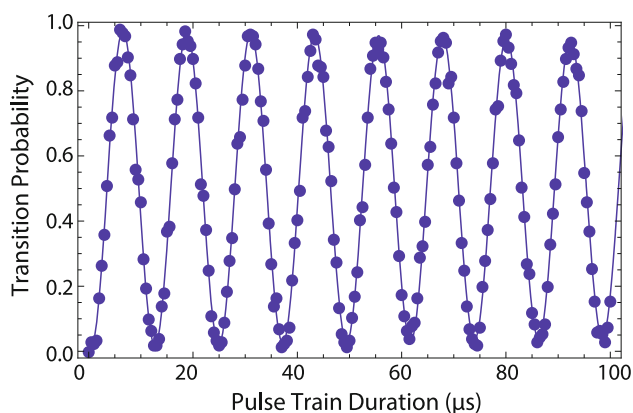


Fig. 7 Rabi oscillations driven by a pair of copropagating combs with an AOM shift between them. In these data, the laser repetition frequency is directly stabilized

$k \in \mathbb{Z}$. Figure 7 shows Rabi flopping driven by two offset optical frequency combs, in a copropagating geometry where the repetition rate is directly stabilized.

The Rabi frequency for the case of two offset combs is exactly as written for the case of a single comb (Eq. 22), where this time $g_0^2 = (\bar{I}/2I_{\text{sat}})\gamma^2$ characterizes the intensity \bar{I} of each of the two combs. For the offset combs, the four-photon AC Stark shift is modified from the asymmetry in the spectrum of two-photon beat notes. Once again summing over all non-resonant beat notes, we find

$$\begin{aligned} \delta_4 &= - \sum_{\substack{j=-\infty \\ j \neq n}}^{\infty} \frac{\Omega_j^2}{2(j\omega_{\text{rep}} + \omega_A - \omega_q)} - \sum_{j=-\infty}^{\infty} \frac{\Omega_j^2}{2(j\omega_{\text{rep}} + \omega_A + \omega_q)} \\ &= - \frac{\Omega_0^2}{2\omega_{\text{rep}}} \left[\sum_{\substack{j=-\infty \\ j \neq 0}}^{\infty} \frac{\text{sech}^2[(j+n)\omega_{\text{rep}}\tau/2]}{j} \right. \\ &\quad \left. - \sum_{j=-\infty}^{\infty} \frac{\text{sech}^2[(j-n)\omega_{\text{rep}}\tau/2]}{j+2\sigma} \right] \end{aligned} \quad (30)$$

$$\frac{\Omega_0^2}{2\omega_{\text{rep}}} \left[3.412\omega_q\tau + \text{sech}^2(\omega_q\tau/2) \left(\frac{1}{2\sigma} + \frac{1}{1+2\sigma} + \frac{1}{2\sigma-1} \right) \right] \quad (31)$$

where $\tilde{\omega}_A = \omega_A \pmod{\omega_{\text{rep}}}$, and $\sigma \equiv \tilde{\omega}_A/\omega_{\text{rep}}$ is the fractional number of comb teeth that the two combs are offset ($0 < \sigma < 1$ and $\sigma \neq 0.5$), and again we assume $\omega_{\text{rep}}\tau \ll 1$. The extra terms in the Stark shift compared to the single comb case (Eq. 28) account for the closer asymmetric beat notes. Interestingly, the net four-photon AC Stark shift can be nulled by choosing a particular offset frequency for a given pulse duration. In the $^{171}\text{Yb}^+$ system for example, we find that a value of $\sigma \sim 0.35$ (0.40) nulls the Stark shift for pulse duration $\tau \approx 5$ (10) ps. For infinitesimally short

pulses ($\tau \rightarrow 0$), the Stark shift vanishes at the value $\sigma = 1/\sqrt{12}$.

3 Entanglement of spin and motion

The above section treated spin flips from copropagating pulses. Consider now a pair of counterpropagating pulse trains, as shown in Fig. 8. The pulses are timed such that they arrive at the ion simultaneously, and the entire train has effective pulse area of order π . The frequency space picture is the same as shown in Fig. 6b—the two combs have a relative frequency shift, such that there exist pairs of comb lines that match the qubit splitting. However, absorption from one comb and emission into the other now leads to momentum transfer. Moreover, the direction of the momentum transfer is spin-dependent, leading to a spin–motion coupling. The form taken by that coupling will differ based on the duration of the pulse train. If the pulse train is much faster than the trap period, the result will be a spin-dependent kick: $|0\rangle$ and $|1\rangle$ will receive momentum kicks in opposite directions. If the pulse train is much slower than the trap period on the other hand, motional sidebands will be resolved. In the Lamb-Dicke limit where the ion motion is confined much smaller than the optical wavelength, the motion will not be changed when on resonance, while a phonon will be added or subtracted when the beat note between the combs is detuned by the trap frequency.

To understand this process, first consider the effect of a single pair of pulses that arrive simultaneously on the ion from opposite directions. If the two pulses have orthogonal linear polarizations which are mutually orthogonal to the quantization axis ($\text{lin} \perp \text{lin}$), then transitions can only be driven via the polarization gradient created by the two pulses. The Rabi frequency then acquires a sinusoidal position dependence. Under the instantaneous pulse approximation ($\tau = 0$), the Hamiltonian for the ion-pulse interaction becomes:

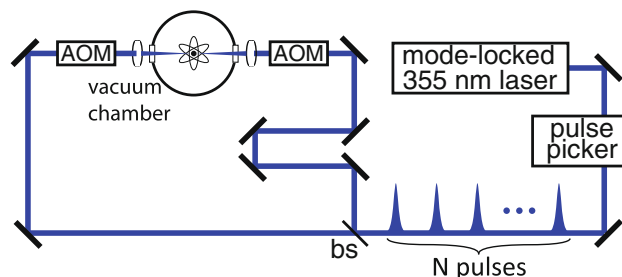


Fig. 8 Experimental layout for counterpropagating geometry. The pulse train is split, and a frequency shift between the two arms is imparted by AOMs

$$H = -\frac{\theta}{2}\delta(t - t_0) \sin[\Delta k\hat{x} + \phi(t_0)]\hat{\sigma}_x \tag{32}$$

where θ is again the total pulse area, t_0 is the arrival time of the pulse pair, Δk is the difference in wavevectors, \hat{x} is the position operator for the ion, and $\phi(t_0)$ is the phase difference between the pulses. The time dependence of this phase difference comes from the AOM frequency shift:

$$\phi(t) = \omega_A t + \phi_0 \tag{33}$$

where ϕ_0 is assumed to be constant over the course of one experiment. Equation 32 can be directly integrated to obtain the evolution operator for a single pulse arriving at time t_0 :

$$U_{t_0} = \exp\left(-i \int H(t) dt\right) = e^{i\frac{\theta}{2} \sin(\Delta k\hat{x} + \phi(t_0))\hat{\sigma}_x} \tag{34}$$

$$= \sum_{n=-\infty}^{\infty} e^{in\phi(t_0)} J_n(\theta) D[in\eta] \hat{\sigma}_x^n \tag{35}$$

where J_n is the Bessel function of order n , D is the coherent state displacement operator [41], and η is the Lamb-Dicke parameter. If we do not assume instantaneous pulses, this result will be modified slightly. However, it will not change the qualitative behavior described below. This is shown in the “appendix”.

Equation 35 consists of operators of the form $D[in\eta]\hat{\sigma}_x^n$, which impart n momentum kicks of size η together with n spin flips. Physically, this corresponds to the process of absorbing a photon from one beam, emitting a photon into the other beam, repeated n times. Each process of absorption followed by emission changes the momentum by η . The amplitude for the n th such process is given by the Bessel function $J_n(\theta)$, together with a phase factor. The net action of this operator on a spin state $|0\rangle$ and coherent motional state $|\alpha\rangle$ is therefore to create a superposition of states of different size kicks, with alternating spin states. This is shown graphically in Fig. 9b.

This behavior can be understood as the scattering of the atomic wavepacket off the standing wave of light, known as Kapitza-Dirac scattering [42–44]. It has been directly observed in atomic beams [43, 44]. It is also similar to the behavior observed in δ -kicked rotor experiments [45]. However, all of the work cited above dealt only with atomic motion; the interaction described here is complicated by the presence of the spin operator.

The evolution operator O_N for a train of N pulses will consist of a sequence of operators of the form 35, separated by free evolution:

$$O_N = U_{t_N} \dots U_{FE}(t_3 - t_2) U_{t_2} U_{FE}(t_2) U_{t_1} \tag{36}$$

where t_n is the arrival time of the n th pulse, and $U_{FE}(T)$ is the free evolution operator for time T , given by:

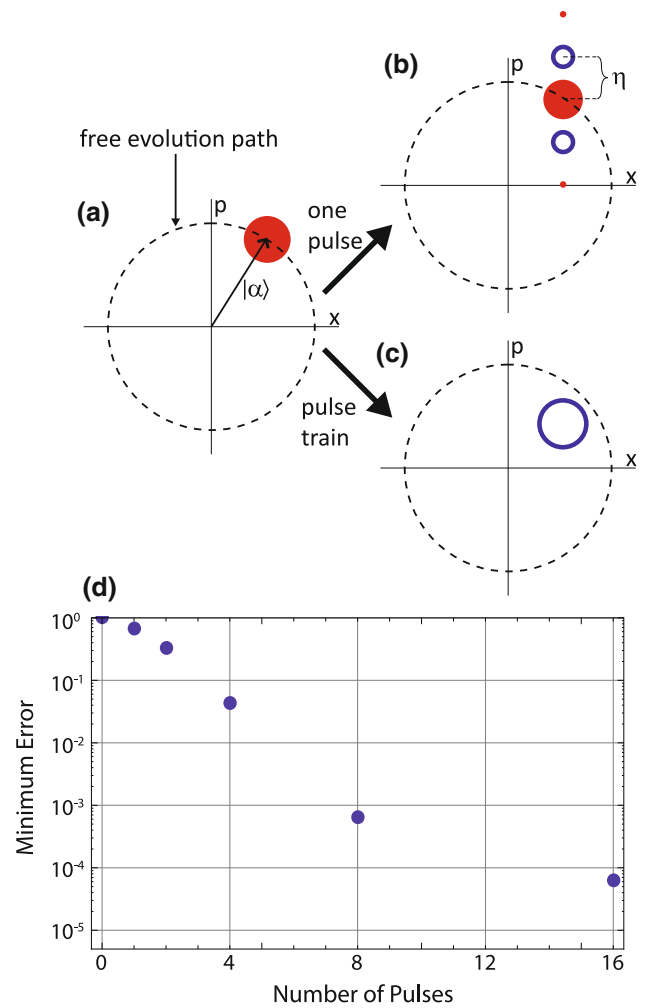


Fig. 9 Phase space diagrams of pulse action. Red closed circles indicate $|0\rangle$, while blue open circles indicate $|1\rangle$. The size of the circle indicates the population in that state. **a** Phase space diagram of an ion initially in the state $|0\rangle|\alpha\rangle$. **b** Upon the arrival of a pulse pair, the ion is diffracted into a superposition of states as in Eq. 35. **c** After N pulse pairs satisfying Eq. 47, population coherently accumulates in the state $|1\rangle|\alpha - i\eta\rangle$ and no other state, as in Eq. 46. Similarly, population initially in $|1\rangle|\alpha\rangle$ coherently accumulates in $|0\rangle|\alpha + i\eta\rangle$. **d** Theoretical error (1-fidelity) of (c) as a function of N . The convergence is very fast—4 pulses is 96 %, 8 pulses 99.9 %, and 16 pulses 99.99 %

$$U_{FE}(T) = e^{-i\omega_{\text{trap}} T a^\dagger a} e^{-i\omega_q T \hat{\sigma}_z / 2} \tag{37}$$

Let the total pulse train area be given by Θ , so that a single pulse area is $\theta = \Theta/N$. Assume that N is sufficiently large such that the single pulse evolution operator in Eq. 35 can be approximated to first order in $1/N$:

$$U_{t_k} \approx 1 + \frac{i\Theta}{2N} \left(e^{i\phi(t_k)} D[i\eta] + e^{-i\phi(t_k)} D[-i\eta] \right) \hat{\sigma}_x \tag{38}$$

The free evolution between the pulses can be absorbed into the pulse operator by transforming to the interaction picture. Define:

$$q_{\pm} = \omega_q \pm \omega_A \tag{39}$$

$$= \cos \frac{\Theta}{2} + i \sin \frac{\Theta}{2} (e^{i\phi_0} D[i\eta] \hat{\sigma}_+ + e^{-i\phi_0} D[-i\eta] \hat{\sigma}_-) \tag{45}$$

In the interaction picture, U_{t_k} becomes:

$$V_{t_k} = U_{FE}^\dagger(t_k) U_{t_k} U_{FE}(t_k)$$

$$= 1 + \frac{i\Theta}{2N} \{ e^{i\phi_0} D[i\eta e^{i\omega_{trap} t_k}] \tag{40}$$

$$\times (e^{iq_+ t_k} \hat{\sigma}_+ + e^{iq_- t_k} \hat{\sigma}_-) + \text{H.c.} \}$$

Under this transformation, the interaction picture pulse train operator becomes:

$$\tilde{O}_N = \prod_{k=N}^1 V_{t_k} \tag{41}$$

There will now be two different approximations made in the fast regime ($\omega_{trap} t_N \ll 1$) and the slow regime ($\omega_{trap} t_N \gg 1$).

3.1 Fast regime

In the fast regime, $\omega_{trap} \approx 0$ during the pulse train, so that the ion is effectively frozen in place. Equation 40 then becomes:

$$V_{t_k} = 1 + \frac{i\Theta}{2N} (e^{i\phi_0} D[i\eta] (e^{iq_+ t_k} \hat{\sigma}_+ + e^{iq_- t_k} \hat{\sigma}_-) + \text{H.c.}) \tag{42}$$

The net pulse train operator for a series of fast pulses (Eq. 41) will then be a product of the V_{t_k} in Eq. 42. In general, this product will be extremely complicated. When expanded, the coefficients of each spin/motion operator will consist of terms of the form $\sum e^{iq_{\pm} t_k}$. Typically the norm of such sums is $\lesssim 1$. For large N , the $1/N$ suppression will result in $\tilde{O}_N \approx 1$, i.e., the pulses do nothing. However, suppose $q_+ t_k / 2\pi \in \mathbb{Z}$ for all pulses, while $q_- t_k / 2\pi \notin \mathbb{Z}$. The pulses are then resonant—in frequency space, this is equivalent to satisfying the bottom sign resonance condition in Eq. 29, but not the top sign. The q_+ terms in the product in Eq. 41 will then coherently add, while the q_- terms will not. As the number of pulses grows, the non-resonant terms are strongly suppressed and can be discarded. In frequency space, this is equivalent to the statement that the comb lines narrow with increasing N , resulting in decreased amplitude for non-resonant processes. Equation 42 therefore becomes:

$$V_{t_k} = 1 + \frac{i\Theta}{2N} (e^{i\phi_0} D[i\eta] \hat{\sigma}_+ + e^{-i\phi_0} D[-i\eta] \hat{\sigma}_-) \tag{43}$$

The pulse train operator is now a product of identical operators:

$$\tilde{O}_N = \left(1 + \frac{i\Theta}{2N} (e^{i\phi_0} D[i\eta] \hat{\sigma}_+ + e^{-i\phi_0} D[-i\eta] \hat{\sigma}_-) \right)^N$$

$$\xrightarrow{N \rightarrow \infty} \exp \left(\frac{i\Theta}{2} (e^{i\phi_0} D[i\eta] \hat{\sigma}_+ + e^{-i\phi_0} D[-i\eta] \hat{\sigma}_-) \right) \tag{44}$$

For a total pulse area of $\Theta = \pi$, Eq. 45 becomes:

$$\tilde{O} = i e^{i\phi_0} D[i\eta] \hat{\sigma}_+ + i e^{-i\phi_0} D[-i\eta] \hat{\sigma}_- \tag{46}$$

This is the desired spin-dependent kick operator. In summary, if the following conditions are satisfied:

$$\frac{q_+ t_k}{2\pi} \in \mathbb{Z} \tag{47}$$

$$\frac{q_- t_k}{2\pi} \notin \mathbb{Z} \tag{48}$$

then in the limit $N \rightarrow \infty$, a pulse train will create a spin-dependent kick in which $|0\rangle$ is kicked up and $|1\rangle$ is kicked down. Alternatively, we could have chosen $q_- t_k / 2\pi \in \mathbb{Z}$ and $q_+ t_k / 2\pi \notin \mathbb{Z}$, in which case the final kick directions would be reversed. In essence, Eq. 47 says that for every pulse, the phase accumulated due to qubit precession ($\omega_q t_k$) plus that accumulated due to the RF modulation on the AOMs ($\omega_A t_k$) should be a multiple of 2π . If the pulses are equally spaced, then $t_k = 2\pi k / \omega_{rep}$, and Eq. 47 is equivalent to Eq. 29. It is also important to note that this spin-dependent kick does not depend on being in the Lamb-Dicke regime.

The condition that only one of q_+ or q_- is resonant is equivalent to the condition that the hyperfine frequency not be an integer or half-integer multiple of the repetition rate:

$$\omega_q \neq \frac{n\omega_{rep}}{2}, n \in \mathbb{Z} \tag{49}$$

If ω_q / ω_{rep} is a half-integer or integer, then it is impossible to be resonant with a kick in one direction without also being resonant with a kick in the opposite direction. The net result will be that the kicks will cancel, and the pulse train will not drive any transitions at all.

It is clear from the time domain analysis that these pulses do not have to be equally spaced. Indeed, numerical optimization shows that the best SDK fidelity is achieved for unequally spaced pulses. To understand this result, consider the product in Eq. 41 to lowest order in Θ/N :

$$\tilde{O}_N = 1 + \frac{i\Theta}{2N} \left\{ \left[e^{i\phi_0} D[i\eta] \left(\sum_{k=1}^N e^{iq_+ t_k} \right) \hat{\sigma}_+ + \text{H.c.} \right] \right.$$

$$\left. + \left[e^{i\phi_0} D[i\eta] \left(\sum_{k=1}^N e^{iq_- t_k} \right) \hat{\sigma}_- + \text{H.c.} \right] \right\}$$

$$+ O((\Theta/N)^2) \tag{50}$$

When the resonance condition in Eq. 47 is satisfied, then the coefficients $\sum_{k=1}^N e^{\pm iq_+ t_k} = N$, and the top term in brackets generates the spin-dependent kick. The bottom term, corresponding to the “wrong way” kick, will lead to infidelity in the SDK. Above it was stated that the

coefficient $\sum_{k=1}^N e^{\pm iq - t_k}$ is $O(1)$ when off resonance, leading to strong suppression for large N . However, maximal suppression occurs when this term is zero. This leads to the condition:

$$\sum_{k=1}^N e^{iq - t_k} = 0 \quad (51)$$

Note that this is a second condition on the arrival times t_k (the first condition being the ordinary resonance condition in Eq. 47). Finding t_k which satisfy both of these conditions will result in a significantly improved SDK fidelity, as compared to satisfying resonance only. However, in general an equally spaced pulse train will not satisfy Eq. 51. This is why using an unequally spaced pulse train can allow higher SDK fidelity—it allows satisfying both Eq. 47 and Eq. 51.

Note that even with satisfying both the conditions mentioned, the SDK fidelity will still not be 1, as Eq. 50 is only to first order in Θ/N . Higher-order terms will lead to infidelity. These terms will also have conditions under which they are zero. By numerically optimizing the arrival times t_k , the SDK infidelity can be suppressed to a very high order with only a small number of pulses. Ultimately, the degree to which the unwanted terms can be suppressed is limited by the number of degrees of freedom available in choosing the pulse arrival times.

Figure 9d shows the numerically optimized fidelity for different numbers of pulses, allowing unequal spacings. Because the pulse train is generated with delay lines (see below), the 8 pulse train has only 3 free parameters. Nevertheless, simulations show that a fidelity better than 99.9 % is achievable after only 8 pulses. With 16 pulses, the fidelity can be better than 99.99 %. Here the AOM difference frequency is fixed. Higher AOM frequencies could potentially allow even higher fidelities.

In order for the approximation $\omega_{\text{trap}} \approx 0$ to be valid, the duration of the pulse train must be at least 2–3 orders of magnitude shorter than the trap period. A typical trap period if of order $1\mu\text{s}$, meaning the pulse train cannot be longer than a few nanoseconds. However, the repetition rate of pulses produced by the available lasers is only 80–120 MHz. At that rate, the ion would experience significant trap evolution even over the course of a small number of pulses. As an alternative, a single pulse from the laser followed by a sequence of delay lines can create a very fast pulse train, as shown in Fig. 10. The limitation on the speed is then determined by the AOM frequency.

We demonstrated in [11] the creation of a spin-dependent kick of the form in Eq. 46. There, we showed that such kicks entangle the spin with the motion, while a second kick can disentangle the motion at integer multiples of the trap period.

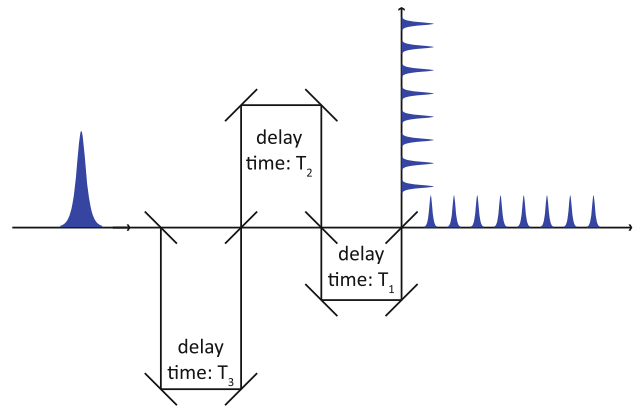


Fig. 10 Optical layout for creating fast pulse train from a single pulse

Direct observation of the motional state of a trapped ion is extremely difficult, and motional information is typically determined by mapping to the spin [46]. Therefore, to detect that we created the operator in Eq. 46, it is necessary to infer the motional entanglement from its impact on the measured spin state. To do this, we performed a Ramsey experiment using microwaves. The experimental sequence was to (1) Initialize the spin state to $|0\rangle$, (2) Perform a $\pi/2$ rotation using near resonant microwaves, (3) Perform a spin-dependent kick using a single pulse through the interferometers, (4) Wait a time T_{delay} (5) Perform a second spin-dependent kick, (6) Perform a second $\pi/2$ rotation, and (7) measure the state of the ion. The frequency of the microwaves was then scanned. If the motion is disentangled from the spin, the result should be full contrast of the Ramsey fringe. On the other hand, if the spin and motion are entangled, then the trace over the motion will destroy the phase coherence. The result will be no Ramsey fringes. The motion should disentangle when T_{delay} matches an integer multiple of the trap frequency.

Figure 11 shows the results of this experiment. Plotted is the Ramsey contrast as a function of T_{delay} . The clear collapse and revival of contrast is a strong indicator that the pulses are indeed performing the spin-dependent kick in Eq. 46. This sort of interferometry is similar to that discussed in [34].

3.2 Slow regime

In the slow regime, the pulse train is much longer than the trap cycle time: $t_N \gg 1/\omega_{\text{trap}}$. Now assume that the ion is in the Lamb-Dicke regime: $\eta\sqrt{n+1} \ll 1$. In this regime, the following approximation can be made:

$$D[i\eta e^{i\omega_{\text{trap}} t_k}] \approx 1 + i\eta(e^{i\omega_{\text{trap}} t_k} a^\dagger + e^{-i\omega_{\text{trap}} t_k} a) \quad (52)$$

where a and a^\dagger are the harmonic oscillator annihilation and creation operators. Substituting this approximation into Eq. 40 yields:

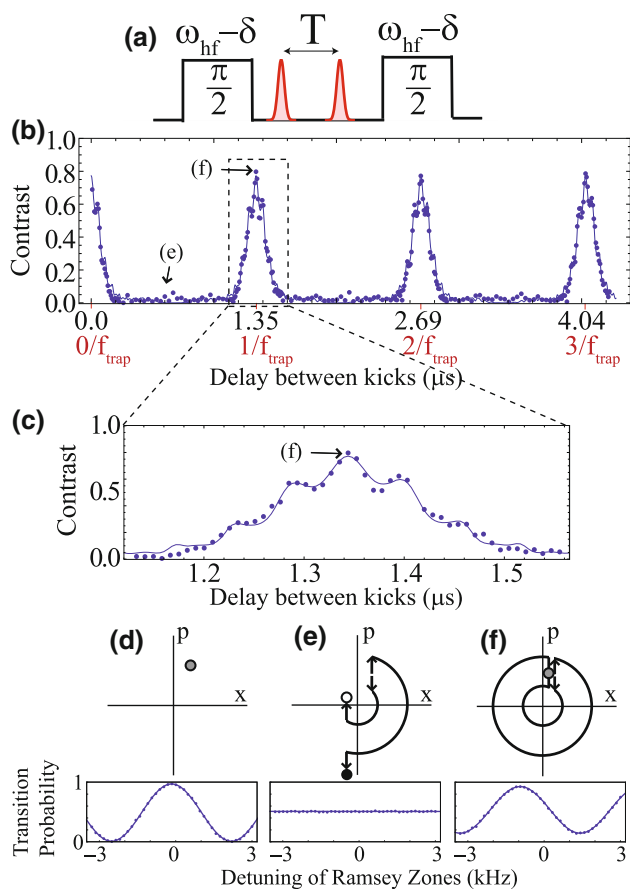


Fig. 11 (Reproduced from [11]). **a** Ramsey experiment to measure effect of spin-dependent kicks. Two spin-dependent kicks separated by a time T are placed between two microwave $\pi/2$ pulses. **b** Ramsey contrast as a function of delay between kicks. Clear revivals of contrast are seen at integer multiples of the trap period. **c** Close up of one revival peak. The small modulation present in the peak is due to uncompensated micromotion. The width of the peak is a function of the ion temperature and the micromotion amplitude. **d–f** Phase space representation at various points on the plot in **(a)**. Also shown are the Ramsey frequency scans at those points, showing the presence or lack of contrast

$$V_{t_k} = 1 + \frac{i\Theta}{2N} \times \{ e^{i\phi_0} (1 + i\eta (e^{i\omega_{\text{trap}} t_k} a^\dagger + e^{-i\omega_{\text{trap}} t_k} a)) \times (e^{iq_+ t_k} \hat{\sigma}_+ + e^{iq_- t_k} \hat{\sigma}_-) + \text{H.c.} \} \quad (53)$$

There are now six phases to consider, associated with six different operators: $e^{iq_\pm t_k}$, $e^{i(q_\pm + \omega_{\text{trap}})t_k}$, and $e^{i(q_\pm - \omega_{\text{trap}})t_k}$. The situation is then similar to the strong pulse regime: If one of these phases satisfies resonance (i.e., equal to 1 for all t_k) while the others do not, then the other terms will be negligible in the limit of large numbers of pulses. For example, suppose that $(q_+ + \omega_{\text{trap}})/2\pi \in \mathbb{Z}$, while none of the other phase terms satisfy this condition. In that case, Eq. 53 becomes:

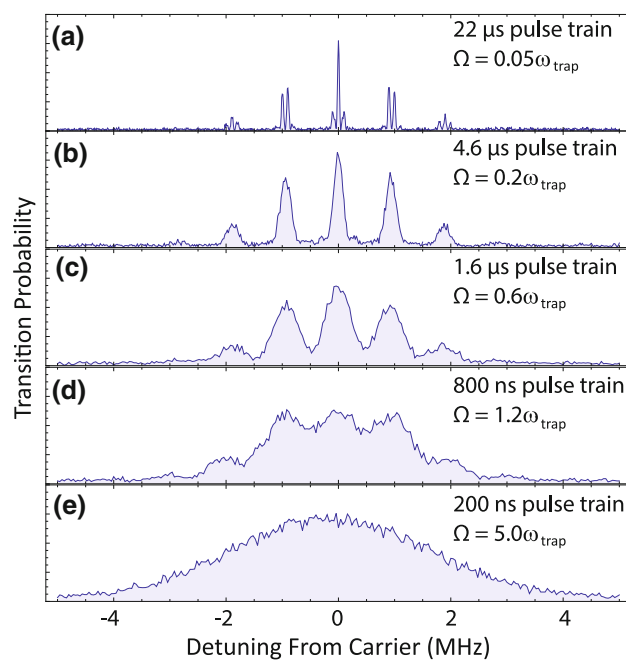


Fig. 12 Data showing the crossover between the slow, resolved sideband regime and the fast, impulsive regime. Each plot corresponds to scanning the frequency of an AOM in one of the arms of counterpropagating pulse trains. **a** $\Omega \ll \omega_t$, and sideband transitions are clearly resolved. **b–d** As the pulse train power is turned up and the Rabi frequency increases, the lines begin to blur together. **e** No features are resolved at all, meaning all sidebands are being driven

$$V_{t_k} = 1 + \frac{i\Theta\eta}{2N} (ie^{i\phi_0} a^\dagger \hat{\sigma}_+ - ie^{-i\phi_0} a \hat{\sigma}_-) \quad (54)$$

As in the fast regime, the pulse train operator in Eq. 41 is now the product of identical operators and converges to:

$$\tilde{O} = \cos \frac{\Theta\eta}{2} + i \sin \frac{\Theta\eta}{2} (ie^{i\phi_0} a^\dagger \hat{\sigma}_+ - ie^{-i\phi_0} a \hat{\sigma}_-) \quad (55)$$

This is Rabi flopping on the blue sideband. Similarly, the other resonance conditions correspond to red sideband and carrier operations. This behavior is shown in Fig. 12a.

We previously reported in [9] on using pulse trains to do resolved sideband operations, as described above. There we demonstrated sideband cooling and two ion entanglement using the Mølmer-Sørensen technique [16, 28, 47].

Figure 12 is experimental data showing the crossover between the slow and fast regimes. In these data, the transition probability was measured as a function of AOM detuning. In (a), sideband features are clearly resolved. The peaks correspond to the carrier and sidebands at each of the three trap frequencies (1.0, 0.9, 0.1) MHz. These transitions follow from Eq. 53. As the power is increased and the pulse train duration decreased, the sidebands become less resolved, as the behavior crosses over from the slow regime to the fast regime. In (e), all of this structure has been

washed out, and the motional transition is now described by impulsive kicks. From a sideband perspective, all sidebands are being driven simultaneously.

4 Ultrafast gates

The goal of creating spin-dependent kicks of the form in Eq. 46 is to execute a fast two ion entangling gate. Such a gate would not be based on sidebands and would therefore be fundamentally different from previously implemented two ion gates. Because it does not depend on addressing sidebands, such a gate will be temperature insensitive and would not require the ion to be cooled to the motional ground state or even cooled to the Lamb-Dicke regime. Additionally, the Raman lasers generating the spin-dependent kick can be focused down to address just two adjacent ions in a long chain. If the gate is sufficiently fast, the other ions do not participate in the interaction. In principle, this allows this type of gate to be highly scalable. There have been theoretical proposals for such a gate in [48] and in [49]. Both schemes rely on using a sequence of spin-dependent kicks, timed such that the collective motion returns to its original state at the end of the process. This leaves a spin-dependent phase.

To understand the origin of this spin-dependent phase, consider a simple sequence of three spin-dependent kicks applied to two ions:

1. $t = 0$: momentum kick of size $+\Delta k$
2. $t = T$: momentum kick of size $-2\Delta k$
3. $t = 2T$: momentum kick of size $+\Delta k$

This is a simplified version of the scheme proposed by Duan [49]. Suppose that the total length of the kicking sequence is much faster than the trap period: $\omega_{\text{trap}}T \ll 1$. In that case, trap evolution during the kicks can be ignored, and the ions behave as free particles. The first kick imparts a momentum to each ion of Δk . The ions then move at a constant velocity away from equilibrium, until the second kick reverses the direction. The third kick then stops the motion of the ions at (nearly) the original position.

For two ions, there are four different possible spin states. Each will have a different motional excitation in response to these kicks, as shown in Fig. 13a.

If the ion spin state is $|0\rangle|0\rangle$ or $|1\rangle|1\rangle$, the two ion energy from the Coulomb interaction does not change during the sequence. However, for $|0\rangle|1\rangle$ and $|1\rangle|0\rangle$, the energy changes as the ions get further apart and then closer together. The time-dependent energy difference between these two configurations is:

$$\Delta E(t) = \frac{e^2}{d} - \frac{e^2}{\sqrt{d^2 + \delta(t)^2}} \approx \frac{2e^2\delta(t)^2}{d^3} \quad (56)$$

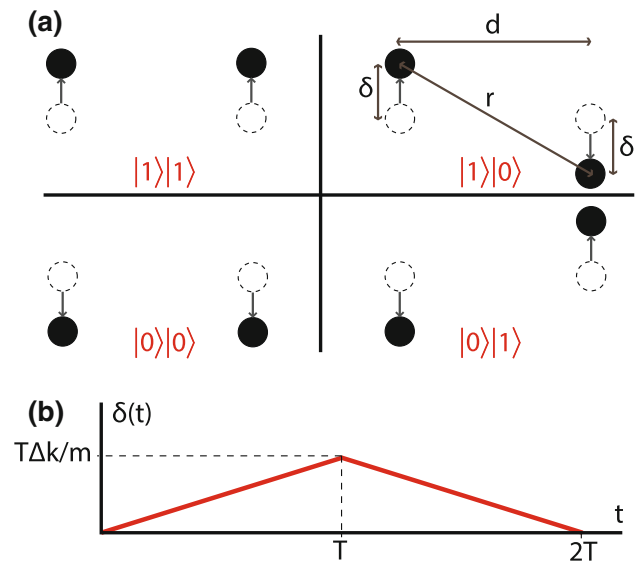


Fig. 13 **a** The ground state of the motion is excited into four different possible configurations depending on the two ion spin state. The *dashed circles* show the original, equilibrium position of the ions. The *arrow and solid circles* show the path followed after the first kick. **b** In the limit where the kicks are much faster than the trap period, the trap evolution during the kicking sequence is negligible, and the ions can be considered as free particles. The displacement δ of each ion from equilibrium as a function of time is shown

where e is the electron charge, d is the distance between the ions in equilibrium, and $\delta(t)$ is the displacement of each ion from equilibrium as a function of time (see Fig. 13b). The acquired phase difference from this process is given by:

$$\Delta\phi = \int_0^{2T} \Delta E(t) dt = \frac{4e^2\Delta k^2 T^3}{3d^3 m^2} \quad (57)$$

We see then that the motional state (nearly) returns to its original state at the end of the process, while $|0\rangle|1\rangle$ and $|1\rangle|0\rangle$ acquire a phase relative to $|0\rangle|0\rangle$ and $|1\rangle|1\rangle$. This is thus a phase gate. Note that the motion is entirely driven. Equation 57 is valid only because the ions are effectively free particles. The natural harmonic motion in the trap does not lead to phase accumulation.

The fidelity of the phase gate described above is limited by free evolution in the trap. Because the gate is not truly instantaneous, there will be a small amount of residual entanglement with the motion at the end of the process. This infidelity can be eliminated by more complex kicking sequences, described below.

Alternatively, this process can be viewed as exciting the two normal modes of motion in the trap. Phase space diagrams of the kick sequence are shown in Fig. 14 for the two different modes (center of mass and relative), both in the non-rotating frame and in the rotating frame. We can determine the evolution of a coherent state $|\alpha\rangle$ subjected to

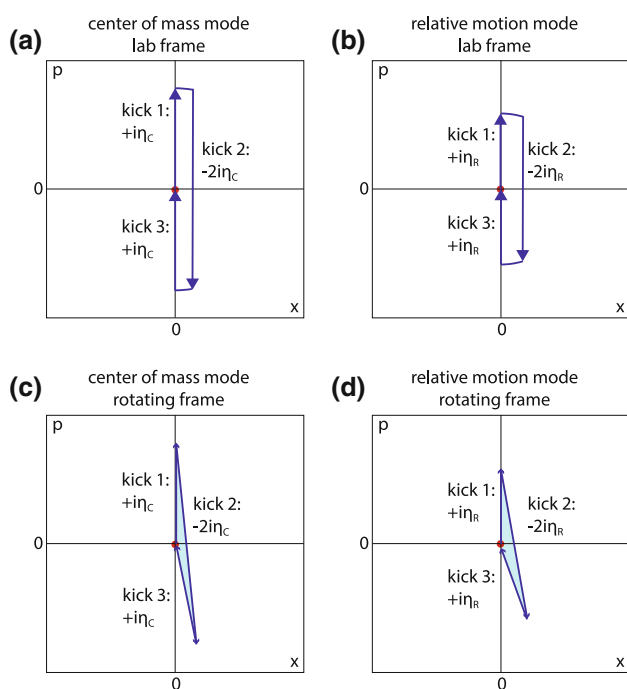


Fig. 14 Phase space picture of the kick sequence described in the text. **a, b** are shown in the non-rotating frame, where free evolution follows circles in phase space. **c, d** are in the rotating frame. The phase difference is given by twice the difference in the enclosed area

the kicks described above. For simplicity in this example, we will treat the ground state $\alpha = 0$.

At the end of the simple pulse sequence, the state of the ions in a normal mode of frequency ω is:

$$e^{i\eta^2(-4\sin(\omega T)+\sin(2\omega T))} |i\eta(1 + (-2 + e^{-i\omega T})e^{-i\omega T})\rangle \quad (58)$$

The phase for a given mode is given by:

$$\phi \approx -\frac{2\Delta k^2 T}{m} \left(1 + \frac{\omega^2 T^2}{3}\right) \quad (59)$$

The phase difference between the two modes is thus given by:

$$\Delta\phi = -\frac{2\Delta k^2 T^3}{3m} (\omega_R^2 - \omega_C^2) \quad (60)$$

$$= \frac{4e^2 \Delta k^2 T^3}{3d^3 m^2} \quad (61)$$

where ω_C and ω_R are the frequencies for the center of mass and relative motion modes. This is the same expression found using the Coulomb picture in Eq. 57.

The phase difference in Eq. 57 can also be extracted by examining the phase space area enclosed by this sequence. The trajectories in the rotating frame are shown in Fig. 14c, d. In the rotating frame all paths are driven, which leads to phase accumulation. If a coherent state is driven through a trajectory which encloses an area A in the rotating frame

phase space, that coherent state acquires a phase $2A$ [50, 51]. This fact allows us to determine the phase acquired simply by calculating the area enclosed in Fig. 14c and d. This calculation once again matches the phase in Eq. 59.

It is worth pointing out that although the simple example illustrated in Fig. 13 uses the transverse modes of motion, such a phase gate also works with the axial modes of motion. Moreover, if the axial modes of motion are used, the displacement δ is directly along the line separating the two ions, resulting in a larger modification of the Coulomb interaction. Equation 61 applies equally for axial or transverse modes. For transverse modes, the term in parentheses is ω_z^2 , while for axial modes it is $2\omega_z^2$. So if all other parameters are held constant there is a factor of 2 greater phase when using axial modes instead of transverse. However, there is added flexibility in using transverse modes, as will be discussed below.

Unfortunately, this simple sequence of kicks has two serious limitations. First, the phase obtained from this sequence is small. Plugging realistic experimental parameters ($d = 5 \mu\text{m}$, $T=100 \text{ ns}$, $\Delta k = 2 \times (\frac{2\pi}{355 \text{ nm}})$) into Eq. 57 we find a phase difference of $\pi/780$, significantly smaller than the $\pi/2$ needed for a maximally entangling phase gate. Second, the motion does not factor completely at the end of the pulse sequence, but some residual entanglement remains. This is clearly seen in Eq. 58 where the final state now depends on η , ω , and T . Both of these limitations can, in principle, be overcome by using more complicated pulse sequences with many laser pulses strung together to give a larger momentum kick.

The theory proposals in [48] and [49] both go beyond the simple pulse sequence presented above. In [49], Duan solves these problems by using many pulses in quick succession. Moreover, he shows that with more complicated pulse sequences the errors can be reduced while still completing the gate in a time much faster than the trap period. This allows the scheme to be used on a pair of adjacent ions in a long chain. If the gate is sufficiently fast, the other ions are not disturbed and the gate is scalable to large ion crystals. Unfortunately, this scheme relies on a very large number of pulses ($>1,000$) in a very short period of time ($<5 \text{ ns}$), and there is not currently a commercial laser available with high enough power and fast enough repetition rate to implement this scheme in our system.

In Garcia-Ripoll [48], the trap evolution is used to control the trajectory in phase space. By correctly choosing the timing of a series of spin-dependent kicks, the relative phase accumulated by the two normal modes can be controlled and both phase space trajectories can be closed, returning the ions to their original position. Here we will present an experimentally achievable extension of their scheme which could perform an entangling phase gate on

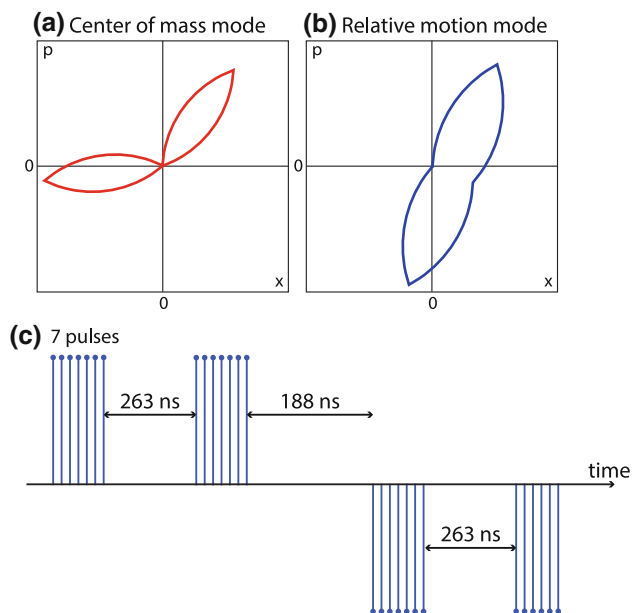


Fig. 15 Phase space picture of an experimentally realizable phase gate. **a** Center of mass mode, **b** relative motion mode. In the rotating frame the direction of the spin-dependent kick rotates at the normal mode frequency. **c** Depiction of kick sequence. The ion is kicked 7 times by 7 successive laser pulses with 12.5 ns of trap evolution between each kick. The ion then evolves in the trap for $t_1 = 263$ ns then kicked 7 more times. After a wait of $t_2 = 188$ ns, the sequence is reversed with 7 kicks in the opposite direction, free evolution for t_1 and a final 7 kicks to return the ions to their original position

two ions in approximately 1 μ s. There have been other proposals of experimentally achievable timings for fast entangling gates, see Bentley [52].

For simplicity, we choose a scheme similar to that in Garcia-Ripoll [48], but to accumulate more phase we replace each of the four spin-dependent-kicks in [48] with 7 spin-dependent kicks. The gate will be executed on transverse motional modes. The advantage of using transverse modes lies in the fact that the frequency ratio between the center of mass and relative modes of motion can be tuned. For the axial modes, that ratio is fixed at $\sqrt{3}$. The transverse center of mass frequency for the gate described here is 1.67 MHz; the relative mode frequency is 1.48 MHz. Experimentally each kick is derived from a single pulse of a mode-locked laser with a repetition rate of 80.16 MHz, so the delay between successive kicks is 12.5 ns. This is not negligible compared to the trap period of 599 ns. As a result, the trap evolution between the kicks is important and must be taken into account. We apply 7 spin-dependent kicks with 7 successive pulses from the laser. Because each kick also flips the spin of the ion, the direction of the spin-dependent kick must be reversed between successive pulses to continue to add momentum to the system. After the 7 spin-dependent kicks, the ion is allowed to evolve in the trap for a time $t_1 = 263$ ns, and

then 7 more spin-dependent kicks are applied in the same direction. The system then evolves freely for a time $t_2 = 188$ ns. The first three steps are then reversed: 7 more kicks in the opposite direction, evolve for t_1 , 7 more kicks to return the system to its original location. The total gate time is 1.02 μ s. Figure 15 shows the path in phase space for both the center of mass and relative modes.

The scheme presented in Fig. 15 is just one of many possible ways to perform this phase gate. There are three constraints. Both the normal mode phase spaces must close, and the differential phase between the two phase spaces must be $\pi/2$. As an added constraint, all the kicks must be spaced by multiples of the fixed laser repetition rate. In a span of 1 μ s, the laser produces 80 pulses. Each pulse can give no momentum kick or a momentum kick of η in either direction. This means that there are $3^{80} = 1.5 \times 10^{38}$ different possible pulse sequences. Most of those do not fulfill the constraints above, but a detailed search reveals that there is a very large set of solutions. However, it is unlikely that there exist solutions much faster than a few hundred nanoseconds using the experimental system presented here, as the algorithm is ultimately limited by the repetition rate of the laser.

5 Conclusion

We have demonstrated that mode-locked lasers are an extremely versatile tool in the coherent control and entanglement of trapped ions in both the fast and slow regimes.

In the slow regime, we have shown that the spectral features of the frequency comb can be used in much the same way as CW lasers, where ion-ion entanglement is produced by addressing sideband transitions. The advantages in this regime are twofold: First, the available power enables operating much further from resonance, which reduces laser-induced decoherence. Second, the broad spectrum allows direct coupling of the qubit levels using a single beam, without the experimental difficulties associated with creating a microwave beat note between two CW beams.

In the fast regime, we have shown that it is possible to drive arbitrary rotations of a trapped ion in tens of picoseconds, which is many orders of magnitude faster than the coherence time. We have also shown the ability to perform fast spin-dependent kicks, which opens the door to performing very fast gates. The advantage of these gates is their insensitivity to temperature, their extreme speed, and their potential for scalability.

Acknowledgments This work is supported by grants from the US Army Research Office with funding from the DARPA OLE program,

IARPA, and the MURI program; the NSF PIF Program; the NSF Physics Frontier Center at JQI; and the European Commission AQ-UTE program.

Appendix: Motional evolution operator with nonzero pulse duration

In Sect. 3, Eq. 35 was derived by approximating the pulse as a δ -function. This section examines the validity of that approximation. The pulse duration is of order 10 ps, meaning it is several orders of magnitude faster than the trap frequency or the AOM frequency. Therefore, the Rosen-Zener solution in Sect. 2 can be used, with $\theta \rightarrow \theta \sin(\Delta k \hat{x} + \phi)$ in Eqs. 5 and 6:

$$A = \frac{\Gamma^2(\xi)}{\Gamma(\xi - \frac{\theta}{2\pi} \sin(\Delta k \hat{x} + \phi)) \Gamma(\xi + \frac{\theta}{2\pi} \sin(\Delta k \hat{x} + \phi))} \quad (62)$$

$$B = -\sin\left(\frac{\theta}{2} \sin(\Delta k \hat{x} + \phi)\right) \operatorname{sech}\left(\frac{\omega_q T_p}{2}\right) \quad (63)$$

The $\hat{\sigma}_x$ term in part of Eq. 4 is given by iB , which can be expanded using the Jacobi-Anger expansion as:

$$iB = \operatorname{sech}\left(\frac{\omega_q T_p}{2}\right) \sum_{\text{oddn}=-\infty}^{\infty} e^{in\phi} J_n(\theta) D[in\eta] \quad (64)$$

This is nearly identical to the $\hat{\sigma}_x$ term in Eq. 35, but with an overall $\operatorname{sech}(\omega_q T_p/2)$ term modifying the populations. The even-order diffraction terms are of order θ^2 or higher, which were assumed to be negligible in Sect. 3. Nonzero pulse duration can thus be accounted for by replacing $\theta \rightarrow \theta \operatorname{sech}(\omega_q T_p/2)$. This will correspond to a slight reduction in the effective pulse area as compared to a δ -function pulse.

References

1. T. Udem, R. Holzwarth, T.W. Hansch, *Nat. Biotechnol.* **416**, 233 (2002)
2. S. Cundiff, J. Ye, *Rev. Mod. Phys.* **75**, 325 (2003)
3. J.L. Hall, *Rev. Mod. Phys.* **78**, 1279 (2006)
4. J.L. Hall, *Rev. Mod. Phys.* **78**, 1279 (2006)
5. M.C. Stowe, A. Pe'er, J. Ye, *Phys. Rev. Lett.* **100**, 203001 (2008)
6. M. Viteau, A. Chotia, M. Allegrini, N. Bouloufa, O. Dulieu, D. Comparat, P. Pillet, *Sci. Agric.* **321**, 232 (2008)
7. D. Press, K.D. Greve, P.L. McMahon, T.D. Ladd, B. Friess, C. Schneider, M. Kamp, S. H'offling, A. Forchel, Y. Yamamoto, *Nat. Photonics.* **4**, 367 (2010)
8. A. Greilich, D.R. Yakovlev, A. Shabaev, A.L. Efros, I.A. Yugova, R. Oulton, V. Stavarache, D. Reuter, A. Wieck, M. Bayer, *Sci. Agric.* **313**, 341 (2006)
9. D. Hayes, D.N. Matsukevich, P. Maunz, D. Hucul, Q. Quraishi, S. Olmschenk, W.C. Campbell, J. Mizrahi, C. Senko, C. Monroe, *Phys. Rev. Lett.* **104**, 140501 (2010)
10. W.C. Campbell, J. Mizrahi, Q. Quraishi, C. Senko, D. Hayes, D. Hucul, D.N. Matsukevich, P. Maunz, C. Monroe, *Phys. Rev. Lett.* **105**, 090502 (2010)
11. J. Mizrahi, C. Senko, B. Neyenhuis, K.G. Johnson, W.C. Campbell, C.W.S. Conover, C. Monroe, *Phys. Rev. Lett.* **110**, 203001 (2013)
12. R. Blatt, D. Wineland, *Nat. Biotechnol.* **453**, 1008 (2008)
13. T.D. Ladd, F. Jelezko, R. Laflamme, Y. Nakamura, C. Monroe, J.L. O'Brien, *Nat. Biotechnol.* **464**, 45 (2010)
14. C.A. Sackett, D. Kielpinski, B.E. King, C. Langer, V. Meyer, C.J. Myatt, M. Rowe, Q.A. Turchette, W.M. Itano, D.J. Wineland, C. Monroe, *Nat. Biotechnol.* **404**, 256 (2000)
15. H. Haffner, W. Hansel, C.F. Roos, J. Benhelm, D.C. al kar, M. Chwalla, T. Korber, U.D. Rapol, M. Riebe, P.O. Schmidt, C. Becher, O. Guhne, W. Dur, R. Blatt, *Nat. Biotechnol.* **438**, 643 (2005)
16. P.C. Haljan, P.J. Lee, K.-A. Brickman, M. Acton, L. Deslauriers, C. Monroe, *Phys. Rev. A* **72**, 062316 (2005)
17. T. Monz, P. Schindler, J.T. Barreiro, M. Chwalla, D. Nigg, W.A. Coish, M. Harlander, W. H'ansel, M. Hennrich, R. Blatt, *Phys. Rev. Lett.* **106**, 130506 (2011)
18. R. Islam, E.E. Edwards, K. Kim, S. Korenblit, C. Noh, H. Carmichael, G.-D. Lin, L.-M. Duan, C.-C.J. Wang, J.K. Freericks, C. Monroe, *Nat. Commun.* **2**, 377 (2011)
19. J.T. Barreiro, M. Muller, P. Schindler, D. Nigg, T. Monz, M. Chwalla, M. Hennrich, C.F. Roos, P. Zoller, R. Blatt, *Nat. Biotechnol.* **470**, 486 (2011)
20. A. Friedenauer, H. Schmitz, J.T. Glueckert, D. Porras, T. Schaetz, *Nat. Phys.* **4**, 747 (2008)
21. S. Gulde, M. Riebe, G.P.T. Lancaster, C. Becher, J. Eschner, H. Haffner, F. Schmidt-Kaler, I.L. Chuang, R. Blatt, *Nat. Biotechnol.* **421**, 48 (2003)
22. K.-A. Brickman, P.C. Haljan, P.J. Lee, M. Acton, L. Deslauriers, C. Monroe, *Phys. Rev. A* **72**, 050306 (2005)
23. P. Schindler, J.T. Barreiro, T. Monz, V. Nebendahl, D. Nigg, M. Chwalla, M. Hennrich, R. Blatt, *Sci. Agric.* **332**, 1059 (2011)
24. R. Ozeri, C. Langer, J.D. Jost, B. DeMarco, A. Ben-Kish, B.R. Blakestad, J. Britton, J. Chiaverini, W.M. Itano, D.B. Hume, D. Leibfried, T. Rosenband, P.O. Schmidt, D.J. Wineland, *Phys. Rev. Lett.* **95**, 030403 (2005)
25. R. Ozeri, W.M. Itano, R.B. Blakestad, J. Britton, J. Chiaverini, J.D. Jost, C. Langer, D. Leibfried, R. Reichle, S. Seidelin, J.H. Wesenberg, D.J. Wineland, *Phys. Rev. A* **75**, 042329 (2007)
26. Q.A. Turchette, Kielpinski, B.E. King, D. Leibfried, D.M. Meekhof, C.J. Myatt, M.A. Rowe, C.A. Sackett, C.S. Wood, W.M. Itano, C. Monroe, D.J. Wineland, *Phys. Rev. A* **61**, 063418 (2000)
27. K. Mølmer, A. Sørensen, *Phys. Rev. Lett.* **82**, 1835 (1999)
28. G. Milburn, S. Schneider, D. James, *Fortschr. Phys.* **48**, 801 (2000)
29. W.K. Hensinger, S. Olmschenk, D. Stick, D. Hucul, M. Yeo, M. Acton, L. Deslauriers, C. Monroe, *Appl. Phys. Lett.* **88**, 034101 (2006)
30. J.P. Home, D. Hanneke, J.D. Jost, J.M. Amini, D. Leibfried, D.J. Wineland, *Sci. Agric.* **325**, 1227 (2009)
31. C. Ospelkaus, U. Warring, Y. Colombe, K.R. Brown, J.M. Amini, D. Leibfried, D.J. Wineland, *Nat. Biotechnol.* **476**, 181 (2011)
32. S. Olmschenk, D.N. Matsukevich, P. Maunz, D. Hayes, L.-M. Duan, C. Monroe, *Sci. Agric.* **323**, 486 (2009)
33. S. Olmschenk, K.C. Younge, D.L. Moehring, D.N. Matsukevich, P. Maunz, C. Monroe, *Phys. Rev. A* **76**, 052314 (2007)
34. J.F. Poyatos, J.I. Cirac, R. Blatt, P. Zoller, *Phys. Rev. A* **54**, 1532 (1996)
35. A. Siegman, *Lasers University Science Books*. Sausalito, CA (1986)
36. N. Rosen, C. Zener, *Phys. Rev.* **40**, 502 (1932)

37. N.V. Vitanov, P.L. Knight, *Phys. Rev. A* **52** 2245 (1995)
38. R.T. Robiscoe, *Phys. Rev. A* **17**, 247(1978)
39. J. Mizrahi, Ph.D. thesis, University of Maryland, College Park (2013)
40. R. Islam, Ph.D. thesis, University of Maryland, College Park (2012)
41. R. Glauber, *Phys. Rev.* **131**, 2766 (1963)
42. P. Kapitza, P. Dirac, *Math. Proc. Camb. Phil. Soc.* **29**, 297 (1933)
43. R.E. Sapiro, R. Zhang, G. Raithel, *Phys. Rev. A* **79**, 043630 (2009)
44. P.L. Gould, G.A. Ruff, D.E. Pritchard, *Phys. Rev. Lett.* **56**, 827 (1986)
45. J.-A. Currivan, A. Ullah, M. Hoogerland, *EPL* **85**, 30005 (2009)
46. D. Leibfried, D.M. Meekhof, B.E. King, C. Monroe, W.M. Itano, D.J. Wineland, *Phys. Rev. Lett.* **77**, 4281 (1996)
47. A. Sorensen, K. Molmer, *Phys. Rev. Lett.* **82**, 1971 (1999)
48. J.J. Garcia-Ripoll, P. Zoller, J.I. Cirac, *Phys. Rev. Lett.* **91**, 157901 (2003)
49. L.-M. Duan, *Phys. Rev. Lett.* **93**, 100502 (2004)
50. A. Luis, *J. Phys J. Phys. A: Math. Gen.* **34**, 7677 (2001)
51. X. Wang, P. Zanardi, *Phys. Rev. A* **65**, 032327 (2002)
52. C.D.B. Bentley, A.R.R. Carvalho, D. Kielpinski, J.J. Hope, *New. J. Phys.* **15**, 043006 (2013)